Vapor-phase synthesis, growth mechanism and thickness-independent elastic modulus of single-crystal tungsten nanobelts

Shiliang Wang[1,2], Guoliang Chen[2], Han Huang[1*], Shujun Ma[1], Hongyi Xu[1],
Yuehui He[2], Jin Zou[1,3]

[1]*School of Mechanical and Mining Engineering, The University of Queensland, QLD 4072, Australia*

[2]*School of Physics and Electronics, State Key Laboratory for Powder Metallurgy, Central South University, Hunan 410083, China*

[3]*Centre for Microscopy and Microanalysis, The University of Queensland, QLD 4072, Australia*

[*]Corresponding author: han.huang@uq.edu.au

Abstract

Single-crystal tungsten nanobelts with thicknesses from tens to hundreds of nanometers, widths of several micrometers, and lengths of tens of micrometers were synthesized using chemical vapor deposition. Surface energy minimization was believed to have played a crucial role on the growth of the synthesized nanobelts enclosed by the low-energy {110} crystal planes of body-centered-cubic structure. The anisotropic growth of the crystallographically equivalent {110} crystal planes could be attributable to the asymmetric concentration distribution of the tungsten atom vapor around the nanobelts during the growth process. The elastic moduli of the synthesized tungsten nanobelts with thicknesses ranging from 65 to 306 nm were accurately measured using a newly developed thermal vibration method. The measured modulus values of the tungsten nanobelts were thickness-dependent. After eliminated the effect of surface oxidization using a core-shell model, the elastic modulus of tungsten nanobelts became constant, which is close to that of the bulk tungsten of 410 GPa.

1. Introduction

Metal nanostructures are important building blocks for nanoscale electronics,[1] optical tags,[2] and mechanical sensors.[3-5] For example, metal nanobelts can be the ideal sensing component for measuring the Casimir force that is an attractive force between two close parallel uncharged conducting plates due to the perturbation of vacuum quantum fluctuation.[3-5] For such an application, a metal nanobelt can be placed on the top of a conductive substrate to form a gap at nanoscale, so the deflection of the nanobelt is used to quantitatively determine the Casimir force. The fabrication of a long, straight and ultrathin nanobelt of atomically smooth surfaces is critical for such sensing, and moreover, the mechanical properties, such as elastic modulus, of the synthesized metal nanobelt must be understood to achieve the accurate measurement of the Casimir force.[5-7]

Top-down approaches, such as bulk micromachining technique,[5] and bottom-up methods, such as solution-based synthesis[8-11] and template-based strategies[12] were previously used to fabricate various metal nanobelts. However, the metal nanobelts fabricated using those methods were insufficiently smooth and often distorted. This would lead to significant errors if they served as the sensing component for measuring the Casimir force, as evidenced in the previous experiments and theoretical modeling.[5-7] Chemical vapor deposition (CVD) is a proven technique for fabricating long and straight metal nanowires with perfect single-crystal structures and smooth surfaces.[13, 14] To use the CVD method to synthesise long, straight and smooth metal nanobelts should be feasible in theory if the thermodynamics and kinetics of growth were well-controlled.[15] However, such synthesis was seldom reported.

The accurate measurement of elastic modulus of nanostructures has been challenging due to the difficulties in manipulating and mounting and the unavailability of standard testing techniques for nanostructures.[16-26] For nanowhiskers, the effects of surface

2

contaminations, defects, and surface stress make such testing even more difficult [25, 26]. Recently, the vibration-based methods were emerged as a valuable tool to determine the elastic moduli of nanobelts/nanowires.[24, 27, 28] In those methods, the nanobelts/nanowires were clamped as cantilevers, and their moduli were then derived from their resonant frequencies being measured, based on the Euler-Bernoulli beam theory.[29, 30] Nevertheless, in practice, the application of the vibration-based methods needs to accurately understand the clamped boundary conditions, and know the geometries and the resonating length of the nanobelt being measured. Any uncertainties may significantly change the vibrational modes of the clamped nanobelts, and thus lead to large measurement errors.[31-35] Therefore, pragmatic and reliable methods for the characterization of mechanical property of nanostructures are still lacked. In this paper, we report our successful synthesis of ultrathin, smooth, straight and long single-crystal tungsten (W) nanobelts using the CVD method and our development of a thermal vibration method for accurately measuring the elastic moduli of the synthesized W nanobelts.

2 Experimental Details

2.1 Synthesis and characterization of W nanobelts

W nanobelts were synthesized in a modified horizontal tube furnace with the similar process for W nanowires.[14] During synthesis, Si substrates (10×10 mm^2) were placed 5 - 50 mm away from the exit of a quartz tube (20 mm in diameter), which was loaded with 10 gram high-purity WO$_3$ powder near the gas exit. The quartz tube was then placed in a horizontal tube furnace (60 mm in diameter, 600 mm in length). At the initial stage of synthesis, high-purity Ar gas was introduced through both inlets (in the quartz and furnace tubes) to purge the system. Following that, the inlet of the internal quartz tube was closed and the furnace was heated to 900 ^{o}C in 90 minutes. At the second stage, H$_2$ gas, with a

constant flow of 300 standard cubic centimeters per minute (sccm) and a pressure of 1 atm, and humid Ar atmosphere, with a constant flow of 30 sccm and a pressure of 1 atm, were introduced into the system. The partial pressure of gaseous H_2O in the humid Ar atmosphere (transiting a water-filled flask at 35 ^{o}C) was about 5 kPa, which is significant higher than the partial press of about 2 kPa for the growth of W nanowires.[14] After maintained the temperature at 900 ^{o}C for 24 hours, the sample cooled down gradually to room temperature inside the furnace.

The morphology, structure and chemical composition of the synthesized W nanobelts were characterized by scanning electron microscopy (SEM; JEOL JSM-7800F, operated at 10 - 25 kV) and transmission electron microscopy (TEM; FEI Tecnai F20, operated at 200 kV) equipped with energy dispersive spectroscopy (EDS).

2.2 Thermal vibration measurement of elastic modulus

The W nanobelts fabricated were ultrasonically dispersed in anhydrous ethanol, and the anhydrous ethanol dispersion was then dripped onto a Si wafer. A W nanobelt was selected and carefully moved to the edge of the Si substrate using an electrochemically etched W tip under a high-magnification optical microscope (Objective: Mitutoyo M Plan APO 50 ×) attached to the Laser Doppler Vibrometer (LDV; Polytec MSA-500).[23] The nanobelt was mounted at the edge of the substrate to form a cantilever by the adhesion between the nanobelt and the Si substrate. The thermal vibrational spectra of the cantilever were recorded using LDV. During the measurement of thermal vibration, the incident laser beam (wavelength λ = 633 nm, power < 1 mW) was focused on the nanobelt through a 50× microscope objective (whose spot diameter of convergent laser beam is 0.9 μm) and was perpendicular to the oscillating nanobelt. The velocity of the nanobelt was then determined from the Doppler shift of the backscattered light.[27] A key advantage of the LDV technique

is the ability to measure the vibrational spectra of a nanobelt cantilever in the spectral range of 0 - 2.5 MHz with high frequency resolution.

After completed the measurement, the nanobelt was moved inside on the substrate to obtain a shortened cantilever, and its thermal vibration was measured by the LDV again. Through repeating this process, a series of vibration spectra of the cantilevers of different lengths, though it was still the same nanobelts, were obtained.

3 Results and discussion

3.1 Morphology and structure

Fig. 1a shows the SEM image of the products deposited on a Si substrate. The products are nanobelts of widths of several micrometers and lengths of tens of micrometers, mixed with nanowires of diameters of tens to hundreds of nanometers. Figs. 1b-d show that three nanobelts are mounted at the edge of a Si substrate by using a micro-manipulator.[36] The three nanobelts in fact represent three typical morphologies of the synthesized nanobelts: the parallelogram with the interior angles of 71° and 109° (Fig. 1b), the isosceles trapezoid with the interior angles of 71°, 109° (Fig. 1c), and the trapezoid with the interior angles of 71°, 109°, 55° and 125° (Fig. 1d). Figs. 1e-g are the end-views of the three nanobelts in Figs. 1b - d, respectively, showing that the nanobelts with the uniform thickness have faceted ends and the hexagonal cross-sections with the included angles of 120°. The W nanowires found in the synthesised products have hexagonal cross-sections with the included angles of 120°, as shown in Figs. 1h and 1i.

To understand the structural and chemical characteristics of synthesized nanostructures, transmission electron microscopy (TEM) equipped with energy dispersive spectroscopy (EDS) was employed. Fig. 2a shows the TEM image of a parallelogram-like W nanobelt of a width of 3 μm and a length of 54 μm. High-resolution TEM (HRTEM) and the

corresponding selected-area electron diffraction (SAED) analyses (Fig. 2b and the inset) confirmed that the nanobelt had a body-centered-cubic (*bcc*) single-crystal structure (*a* =3.165 nm; JCPDS: 04-0806) with the growth direction along the <111> directions, and that the belt plane corresponded to the low-energy crystal planes, {110}. TEM also revealed that, besides nanobelts and nanowires, triangular nanosheets were occasionally observed in the synthesized product, as shown in Fig. 2c. The nanosheets were isosceles triangles with the vertex angle of ~ 71°. SAED analyses (the inset in Fig. 2c) revealed that the nanosheets were single-crystal *bcc*-W. TEM and SAED analyses indicated that the nanosheet planes are {110} crystal planes, and the two equilateral sides are parallel to <111> directions and the base side is parallel to <100>. Fig. 2d is the EDS line-scan of W and O recorded at the edge of a nanobelt (the inset). The surface layer of the nanobelts exhibited to have an oxide layer of thickness of ~ 3 nm. This finding is in good agreement with the previous study, where a layer of WO_3 with a thickness of 3 - 5 nm was formed on the surface of W due to the room-temperature oxidization in air.[37, 38]

3.2 Growth mechanism

According to the Wulff theorem,[39] the crystal nuclei of *bcc*-W, grown in nearly thermal equilibrium, tended to form rhombic dodecahedrons enclosed by 12 rhombic low-energy {110} planes, in order to minimize its surface energy. For these W nuclei, the subsequent one-dimensional (1D) and the two-dimensional (2D) growth would result in the formation of W nanowires and parallelogram-like nanobelts with hexagonal cross-sections, respectively, as illustrated in Fig. 3a and shown in Fig. 1. Besides the rhombic dodecahedrons, the Wulff shapes of W nuclei also included the dodecahedrons or the decahedrons enclosed by the low-energy {110} planes, i.e., dodecahedrons enclosed 6 parallelograms and 6 isosceles trapezoids, as illustrated in Fig. 3b, or the decahedrons enclosed by 7 parallelograms, 2

trapezoids and 1 hexagon shown in Fig. 3c. The subsequent 1D and 2D growth of the dodecahedronal nuclei would lead into the formation of W nanowires and isosceles trapezoidal nanobelts with hexagonal cross-sections, as illustrated in Fig. 3b. The subsequent 1D and 2D growth of the decahedronal nuclei would generate hexagonal nanowires, and trapezoidal nanobelts or triangular nanosheets, as illustrated in Fig. 3c, which are shown in Figs. 1 and 2 too.

The different nanostructures shown Figs. 1 and 2 agree well with the Wullf shapes shown in Fig. 3, which were theoretically predicted based on the thermodynamics. Thus, it is rational to suggest that the principle of surface energy minimization played an important role on the formation of W nanostructures in our study. However, surface energy minimization cannot be used for interpreting the 1D and 2D growth of a *bcc*-W nucleus, because all the {110} crystal planes are crystallographically equivalent. This suggests that the kinetics might affect the morphology of the resultant W nanostructures.

During the vapor-growth process, 2D nucleation probability, P_N, on a crystal plane can be expressed as,[40]

$$P_N = B \exp\left(-\frac{\pi\sigma^2}{k^2 T^2 \ln\alpha}\right), \tag{1}$$

where B is a constant, σ the surface energy of the crystal plane, k the Boltzmann constant, T the absolute temperature, and α the supersaturation ratio defined by $\alpha = P/P_0$ (usually >1), where P is the actual vapor pressure and P_0 the equilibrium vapor pressure corresponding to the temperature T. As for a *bcc*-W crystal nucleus enclosed by {110} crystal planes, the outer surfaces are expected to have the same surface energy and temperature, Therefore, the different nucleation probabilities, which lead to the different growth ratios, are most likely to be resulted from the supersaturation ratio of W atom vapor above the different surfaces of a W nucleus.

In our vapor-deposition system, when the supersaturation of W atom vapor was relatively low, the upper surfaces of a faceted W nucleus on the substrate faced a higher concentration of W atom vapor compared to the side surfaces, and thus gained a higher nucleation probability, i.e. a higher growth ratio. Thus, the nucleus would prefer a rapid 1D growth from the substrate to form a nanowire. On the other hand, when the supersaturation of W atom vapor was relatively high, the side surfaces of the faceted W nucleus could also gain a relatively high growth ratio, i.e., lateral growth. As a consequence, when the concentration of W atoms near the side-surfaces was significantly affected by the neighboring W nuclei or pre-formed crystals, the asymmetric concentration distribution around the faceted nucleus led to deferent lateral growth ratios among different side surfaces, and thus generated a 2D growth to form nanobelts or nanosheets. In summary, a relatively low supersaturation of W atom vapor led to the formation of W nanowires as shown in our previous work,[14] while a relatively high supersaturation favored the growth of W nanobelts as demonstrated in the present work.

3.3 Elastic modulus

The elastic moduli of the nanobelts were measured using the thermal vibration method.[24, 27] Figs. 4a - 4e show the optical micrographs of a nanobelt, which was subsequently clamped at different lengths to form five different cantilevers. The morphologies of the clamped nanobelt could also be directly characterized by using SEM. As an example, Fig. 4f shows the same cantilever as that shown in Fig. 4e. The lengths of the five lengths are 34.1, 27.7, 23.1, 20.3 and 16.1 μm, respectively. Note that these clamp lengths were measured from the edge of the Si substrate to the mid-point of the sloped end of the nanobelt, as shown in Fig. 4f. Figs. 4g and 4h are the top and end views of the nanobelt, respectively, demonstrating that the nanobelt has a uniform width of 2.0 μm and thickness of 74 nm. Fig.

4i confirms that no gap is visible between the nanobelt and the Si substrate, indicating that the cantilever is well mounted. Fig. 4j shows the thermal vibration spectra of the five nanobelt cantilevers, where the resonant frequencies of the five beams are also marked.

It is well documented that if a cantilever is made of a homogeneous material and has a uniform geometry, the elastic modulus of the cantilever, E_{ap}, can be derived from the Euler-Bernoulli beam theory using the following equation,[29, 30]

$$f_i = \frac{\alpha_i^2}{2\pi L^2}\sqrt{\frac{E_{ap}I}{\rho A}}, \quad i = 1, 2, 3, \cdots, \tag{2}$$

where f_i are the resonant frequencies (where i is the mode number), L the length, I the second moment of area, A the area of the cross section, ρ the density of the cantilever, and α_i (= 1.875, 4.694, 7.855, 10.966, … for i = 1, 2, 3, 4, …) are the constants satisfying the transcendental equation of $\cos\alpha_i\cosh\alpha_i + 1 = 0$. Using ρ = 19.3 g/cm^3,[38] the measured length, width and thickness of the cantilever (that are used to calculate I and A) and the resonant frequencies, E_{ap} can be calculated according to Eq. (2). Table 1 shows the moduli of the five cantilevers. The average moduli are 358 (for L_1), 355 (L_2), 355 (L_3), 357 (L_4) and 359 (L_5) GPa, respectively. Obviously, the measured moduli of the five different cantilevers are very close, giving an average value of 357 ± 2 GPa, as they were from the same nanobelt. Note that we took the mid-point of the sloped end as the measurement point for the length, the hexagonal cross-section of the nanobelt as a rectangle, in order to simplify the calculation. The error originated from the simplification is below 1%. The consistent modulus values measured from the same nanobelt of different clamp lengths strongly suggest that the thermal vibration method is highly accurate and reliable. However, it is interesting to note that though consistent in values the measured moduli are significantly lower than the bulk counterpart of ~ 410 GPa.[38] The question that arises is if the measured modulus is the true reflection of the elastic property of the CVD-grown W nanobelts.

As mentioned earlier, TEM and EDS examination revealed that there is a oxide layer of ~3 nm on the nanobelts, which might have affected the measuring result. To remove the effect of surface oxidization, the nanobelt was modeled as a sandwich beam that has a core of W covered by a thin shell of WO_3. Eq. (2) is still valid for a sandwiched structure when $E_{ap}I$ and ρA are replaced by their respective effective values, i.e. $(EI)_{ef}$ and $(\rho A)_{ef}$, expressed as,[29, 30]

$$\left(E_{ap}I\right)_{ef} = \frac{E_{in}bh_c^3}{12} + \frac{E_s h_s \left(6h_c^2 + 12h_c h_s + 8h_s^2\right)}{12},$$ (3a)

and
$$\left(\rho A\right)_{ef} = \rho_c h_c b + 2\rho_s h_s b,$$ (3b)

where h, ρ and E_{in} are the thickness, density and intrinsic elastic modulus, respectively, and the suffixes of c and s denote the core and the shell, respectively. Taking ρ_c = 19.3 g/cm^3,[38] ρ_s = 7.2 g/cm^3,[38] E_s = 100 GPa,[41] h_c = 68 nm, h_s = 3 nm, the effective values, $(EI)_{ef}$ and $(\rho A)_{ef}$ were calculated using Eq. (2). Substituting these two effective values into Eq. (1), the average intrinsic moduli, E_{in-av}, were recalculated for the five different clamp lengths, which are 408 (for L_1), 406 (L_2), 406 (L_3), 407 (L_4) and 410 (L_5) GPa, respectively, also shown in Table 1. These give an average value of 407 ± 2 GPa, which is very close to the value of the bulk W, ~ 410 GPa.[42]

The accuracy of the vibration-based method for measuring the elastic modulus of nanobelts can be affected by the uncertainties from the clamped boundary condition, the uniformity along the axial direction and the resonating length of the clamped nanobelts.[31-34] The effects of those factors were difficult to determine in the previous studies. In this work, we have developed a criterion to examine the effect of these uncertainties with ease.

First, for a well-clamped cantilever with uniform size and structure along the axial direction, the ratios of its resonant frequencies are expressed as,[29]

$$f_1 : f_2 : f_3 : f_4 : \cdots = \alpha_1^2 : \alpha_2^2 : \alpha_3^2 : \alpha_4^2 : \cdots = 6.27 : 17.55 : 34.21 : \cdots . \qquad (4)$$

Inappropriate clamping, non-uniformity in the cantilever geometries and material microstructure (e.g. defects) and surface contamination would cause the measured ratios to deviate from the theoretical ratios in Eq. (4). In our measurement, for the five cantilevers shown in Fig. 4, the measured ratios are 1:6.26:17.58:34.38; 1:6.24:17.65:34.48; 1:6.29:17.59 and 1:6.29, respectively. The excellent agreement between the theoretical and measured ratios indicates that the nanobelt was not only ideally clamped by the adhesion between the nanobelt and the substrate, but should also be very uniform along the axial direction. The maximum discrepancy of 0.5% between the measured and theoretical ratios was most likely caused by the surface contamination, shown in Figs. 4h and 1i.

Second, for the same uniform beam with different resonating lengths, the resonant frequencies and the corresponding resonating lengths, according to Eq. (2), have the following relationship,

$$\left[f_1(L_1) \cdot L_1^2 \right] : \left[f_1(L_2) \cdot L_2^2 \right] : \left[f_1(L_3) \cdot L_3^2 \right] : \left[f_1(L_4) \cdot L_4^2 \right] : \left[f_1(L_5) \cdot L_5^2 \right] : \cdots = 1:1:1:1:1 \cdots . \quad (5)$$

In practical measurement, it was hard to exactly determine the real clamp point of the clamped nanobelts, and thus difficult to accurately measure the resonating length.[32] This would result in significant measurement errors in E_{ap}, as E_{ap} ($\propto L^4$) is extremely sensitive to resonating length. In our test, we could easily determine the real clamp points or the resonating lengths of the clamped nanobelts by comprising the measured and theoretical ratios defined by Eq. (5). In this case, the measured ratios, 1: 0.993: 0.996: 0.998: 1.002, are highly consistent with the theoretical ratios, 1: 1: 1: 1: 1, suggesting that the resonating lengths being measured were accurate.

The measurement errors of our measurement mainly arose from exactly determining the thicknesses and the resonating lengths of the cantilevered nanobelt. The error for the

nanobelt thickness was ± 2 nm (Fig. 4h), which could result in an error of about ± 5% in E for the nanobelt of 74 nm in thickness. The measurement error for the cantilever length by optical microscope was estimated to be ±200 nm (Fig. 4), which might lead to an error of ±3%. In addition, air damping also affected the measurement through its effect on the resonant frequencies, particularly for higher mode frequencies. Fig. 5 shows the vibrational spectra of a nanobelt cantilever measured in ambient environment (760 Torr) and low vacuum (~ 1 Torr). It is seen that the resonant frequencies measured in atmosphere are ~ 1% lower than the respective values measured in vacuum. This agrees with the previously reported effect of air damping on the frequency response of atomic force microscope cantilever beams.[43] Therefore, air damping might result in an underestimation of ~ 2% in E in our measurement.

In this study, 17 W nanobelts of the thickness varied from 65 to 312 nm were measured, and the results are shown in Fig. 6. The modulus values (solid triangles) were directly calculated using Eq. (2) without removing the effect of surface oxidization decreased from ~ 400 to ~ 340 GPa when the nanobelt thickness was reduced from ~ 300 to ~ 60 nm. By using the core-shell model to remove the oxidization effect, the moduli calculated using Eq. (2) are close to that of the bulk W, regardless of nanobelt thickness.

4 Concluding remarks

Single-crystal W nanobelts of thicknesses of tens to hundreds of nanometers, widths of several micrometers, and lengths of tens of micrometers were successfully synthesized using CVD. The anisotropic growth of the crystallographically equivalent {110} crystal planes of the W nanobelts was attributed to the asymmetric concentration distribution of W atom vapor around the nanobelts during growth. The elastic moduli of the synthesized W

nanobelts of thicknesses ranged from 65 to 312 nm were measured using a thermal vibration method. The moduli of the nanobelts obtained from the direct measurement were thickness-dependent. Such size dependency was caused by surface oxidation. Through removing the oxidization effect using a core-shell model, the elastic modulus of the nanobelts was independent on thickness, which is almost the same as that of the bulk tungsten. The long, straight and ultrathin W nanobelts with near-perfect smooth surfaces and uniform geometries along the axial direction can be the ideal sensing component for measuring the Casimir force. The developed vibration method is simple, low-cost and accurate, and is practically applicable for determining the moduli of nanobelts or nanowhiskers.

Acknowledgements

References

[1] Kovtyukhova N I and Mallouk T E 2002 Nanowires as Building Blocks for Self-Assembling Logic and Memory Circuits *Chem. Eur. J.* **8** 4354-63

[2] Keating C D and Natan M J 2003 Striped metal nanowires as building blocks and optical tags *Adv. Mater.* **15** 451-4

[3] Ball P 2007 Fundamental physics: feel the force *Nature* **447** 772-4

[4] Soroush R, Koochi A, Kazemi A S, Noghrehabadi A, Haddadpour H and Abadyan M 2010 Investigating the effect of Casimir and van der Waals attractions on the electrostatic pull-in instability of nano-actuators *Phys. Scr.* **82** 045801

[5] Buks E and Roukes M L 2001 Stiction, adhesion energy, and the Casimir effect in micromechanical systems *Phys. Rev. B* **63** 033402

[6] Neto P A M, Lambrecht A and Reynaud S 2005 Casimir effect with rough metallic mirrors *Phys. Rev. A* **72** 012115

[7] van Zwol P J, Palasantzas G and De Hosson J T M 2007 Roughness corrections to the Casimir force: The importance of local surface slope *Appl. Phys. Lett.* **91** 144108

[8] Xia Y, Xiong Y, Lim B and Skrabalak D S E 2009 Shape-Controlled Synthesis of Metal Nanocrystals: Simple Chemistry Meets Complex Physics? *Angew. Chem., Int. Ed.* **48** 60-103

[9] Jing G Y, Duan H L, Sun X M, Zhang Z S, Xu J, Li Y D, Wang J X and Yu D P 2006 Surface effects on elastic properties of silver nanowires: Contact atomic-force microscopy *Phys. Rev. B* **73** 235409 (6pp)

[10] Petrova H, Perez-Juste J, Zhang Z Y, Zhang J, Kosel T and Hartland G V 2006 Crystal structure dependence of the elastic constants of gold nanorods *J. Mater. Chem.* **16** 3957-63

[11] Sun X M and Li Y D 2005 Cylindrical silver nanowires: Preparation, structure, and optical properties *Adv. Mater.* **17** 2626 - 30

[12] Kubo W, Hayakawa H, Miyoshi K and Fujikawa S 2011 Size-Controlled Simple Fabrication of Free-Standing, Ultralong Metal Nanobelt Array *J. Nanosci. Nanotechnol.* **11** 131-7

[13] Richter G, Hillerich K, Gianola D S, Monig R, Kraft O and Volkert C A 2009 Ultrahigh Strength Single Crystalline Nanowhiskers Grown by Physical Vapor Deposition *Nano Lett.* **9** 3048-52

[14] Wang S L, He Y H, Fang X S, Zou J, Wang Y, Huang H, Costa P M F J, Song M,

Huang B, Y., Liu C T, Liaw P K, Bando Y and Golberg D 2009 Structure and field-emission properties of sub-micrometer-sized tungsten-whisker arrays fabricated by vapor deposition *Adv. Mater.* **21** 2387-92

[15] Dai Z R, Pan Z W and Wang Z L 2003 Novel nanostructures of functional oxides synthesized by thermal evaporation *Adv. Funct. Mater.* **13** 9-24

[16] Wong E W, Sheehan P E and Lieber C M 1997 Nanobeam mechanics: elasticity, strength and toughness of nanorods and nanotubes *Science* **277** 1971-5

[17] Yu M-F, Lourie O, Dyer M J, Moloni K, Kelly T F and Ruoff R S 2000 Strength and Breaking Mechanism of Multiwalled Carbon Nanotubes Under Tensile Load *Science* **287** 637-40

[18] Salvetat J P, Kulik A J, Bonard J M, Briggs G A D, Stöckli T, Méténier K, Bonnamy S, Béguin F, Burnham N A and László F 1999 Elastic Modulus of Ordered and Disordered Multiwalled Carbon Nanotubes *Adv. Mater.* **11** 161-5

[19] Wu B, Heidelberg A and Boland J J 2005 Mechanical properties of ultrahigh-strength gold nanowires *Nat. Mater.* **4** 525-9

[20] Han X D, Zhang Z and Wang Z L 2007 Experimental nanomechanics of one-dimensional nanomaterials by in situ microscopy *NANO* **2** 249-71

[21] Huang Y, Lin J, Zou J, Wang M-S, Faerstein K, Tang C, Bando Y and Golberg D 2013 Thin boron nitride nanotubes with exceptionally high strength and toughness *Nanoscale* **5** 4840-6

[22] Ma S, Wang S, Iacopi F and Huang H 2013 A resonant method for determining the residual stress and elastic modulus of a thin film *Appl. Phys. Lett.* **103** 031603-5

[23] Wang S, He Y, Huang H, Zou J, Auchterlonie J G, Hou L and Huang B 2013 An improved loop test for experimentally approaching the intrinsic strength of alumina nanoscale whiskers *Nanotechnology* **24** 285703

[24] Treacy M M J, Ebbesen T W and Gibson J M 1996 Exceptionally high Young's modulus observed for individual carbon nanotubes *Nature* **381** 678-80

[25] Wang Y B, Wang L F, Joyce H J, Gao Q, Liao X Z, Mai Y W, Tan H H, Zou J, Ringer S P, Gao H J and Jagadish C 2011 Super Deformability and Young's Modulus of GaAs Nanowires *Adv. Mater.* **23** 1356-60

[26] Chen B, Wang J, Gao Q, Chen Y, Liao X, Lu C, Tan H H, Mai Y-W, Zou J, Ringer S P, Gao H and Jagadish C 2013 Strengthening Brittle Semiconductor Nanowires through Stacking Faults: Insights from in Situ Mechanical Testing *Nano Lett.* **13** 4369-73

[27] Biedermann L B, Tung R C, Raman A, Reifenberger R G, Yazdanpanah M M and

Cohn R W 2010 Characterization of silver-gallium nanowires for force and mass sensing applications *Nanotechnology* **21** 305701

[28] Belov M, Quitoriano N J, Sharma S, Hiebert W K, Kamins T I and Evoy S 2008 Mechanical resonance of clamped silicon nanowires measured by optical interferometry *J. Appl. Phys.* **103** 074304

[29] Blevins R D 1979 *Formulas for natural frequency and mode shape* (New York: Van Nostrand Reinhold)

[30] Ma S, Huang H, Lu M and Veidt M 2012 A simple resonant method that can simultaneously measure elastic modulus and density of thin films *Surf. Coat. Technol.* **209** 208-11

[31] Kiracofe D R, Yazdanpanah M M and Raman A 2011 Mass and stiffness calibration of nanowires using thermally driven vibration *Nanotechnology* **22** 295504

[32] Zeng D J and Zheng Q S 2007 Resonant frequency-based method for measuring the Young's moduli of nanowires *Phys. Rev. B* **76** 075417

[33] Perisanu S, Gouttenoire V, Vincent P, Ayari A, Choueib M, Bechelany M, Cornu D and Purcell S T 2008 Mechanical properties of SiC nanowires determined by scanning electron and field emission microscopies *Phys. Rev. B* **77** 165434

[34] Guillon S, Saya D, Mazenq L, Perisanu S, Vincent P, Lazarus A, Thomas O and Nicu L 2011 Effect of non-ideal clamping shape on the resonance frequencies of silicon nanocantilevers *Nanotechnology* **22** 245501

[35] Qin Q, Xu F, Cao Y, Ro P I and Zhu Y 2012 Measuring True Young's Modulus of a Cantilevered Nanowire: Effect of Clamping on Resonance Frequency *Small* **8** 2571-6

[36] Nessim G D, Seita M, Plata D L, O'Brien K P, Hart A J, Meshot E R, Reddy C M, Gschwend P M and Thompson C V 2011 Precursor gas chemistry determines the crystallinity of carbon nanotubes synthesized at low temperature *Carbon* **49** 804-10

[37] Warren A, Nylund A and Olefjord I 1996 Oxidation of tungsten and tungsten carbide in dry and humid atmospheres *Int. J. Refract. Met. Hard Mater.* **14** 345-53

[38] Lassner E and Schubert W D 1998 *Tungsten: Properties, Chemistry, Technology of the Element, Alloys, and Chemical Compounds* (New York: Kluwer Academic/Plenum Publishers)

[39] Pimpinelli A and Jacques V 1998 *Physics of crystal growth* (Cambridge: Cambridge University Press)

[40] Blakely J M and Jackson K A 1962 Growth of Crystal Whiskers *J. Chem. Phys.* **37** 428-30

[41]   Liu K H, Wang W L, Xu Z, Liao L, Bai X D and Wang E G 2006 In situ probing mechanical properties of individual tungsten oxide nanowires directly grown on tungsten tips inside transmission electron microscope *Appl. Phys. Lett.* **89** 221908

[42]   Lowrie R and Gonas A M 1967 Single-crystal elastic properties of tungsten from 24°C to 1800 $^{\circ}$C *J. Appl. Phys.* **38** 4505-9

[43]   Chon J W M, Mulvaney P and Sader J E 2000 Experimental validation of theoretical models for the frequency response of atomic force microscope cantilever beams immersed in fluids *J. Appl. Phys.* **87** 3978-88

Table 1. The moduli, E_{ap}, obtained from the direct measurement and the moduli, E_{in}, calculated using the core-shell model.

L (μm)	$E_{ap}(f_1)$ (GPa)	$E_{ap}(f_2)$ (GPa)	$E_{ap}(f_3)$ (GPa)	$E_{ap}(f_4)$ (GPa)	$E_{ap\text{-}av}$ (GPa)	$E_{in}(f_1)$ (GPa)	$E_{in}(f_2)$ (GPa)	$E_{in}(f_1)$ (GPa)	$E_{in}(f_2)$ (GPa)	$E_{in\text{-}av}$ (GPa)
34.1	357	356	358	360	358	407	406	409	412	408
27.7	354	351	357	360	355	405	400	408	411	406
23.1	354	354	358	—	355	404	404	410	—	406
20.3	356	357	357	—	357	406	408	408	—	407
16.1	358	360	—	—	359	409	411	—	—	410
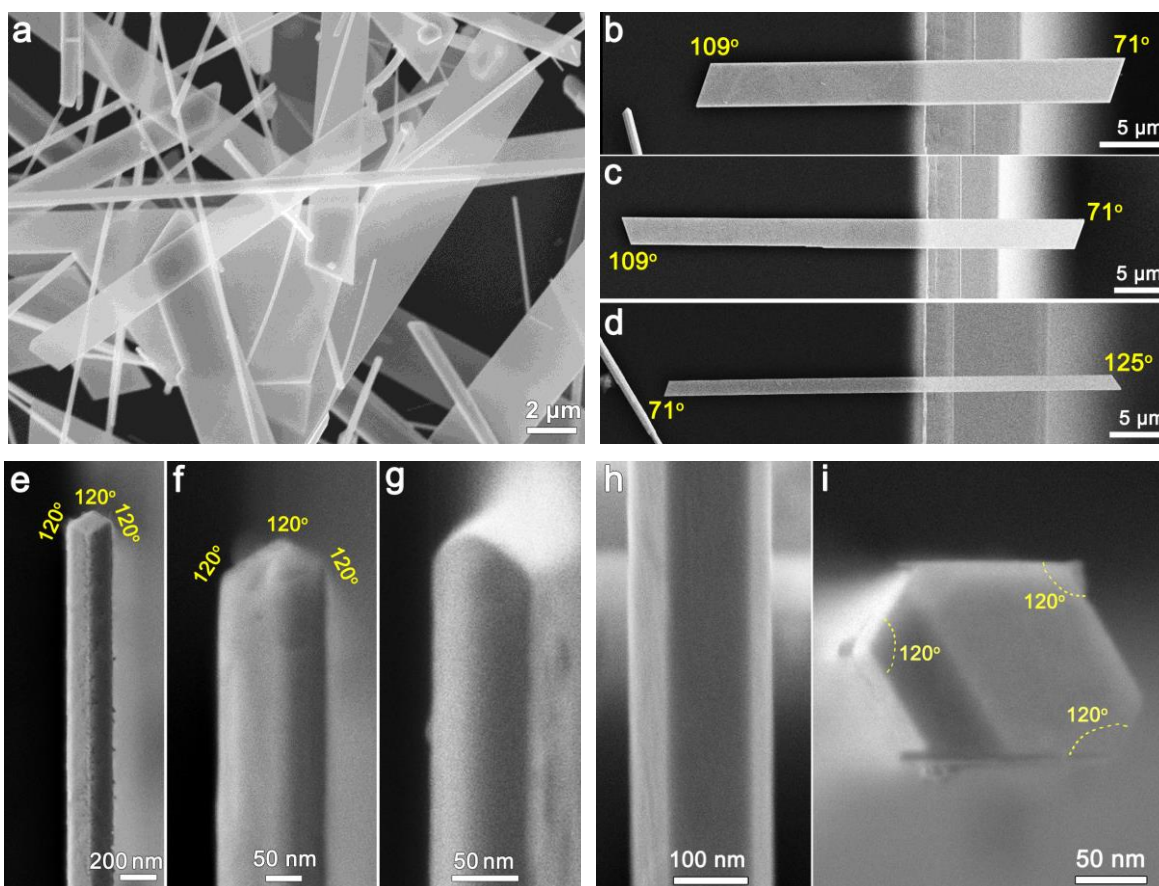
Fig. 1 SEM micrographs of (a) deposited products on the Si wafer; (b-d) W nanobelts mounted at the edge of a Si wafer; (e-g) the respective end-views of the three nanobelts shown in (b-d) ; (h), side-view and (i) end-view of a W nanowire.
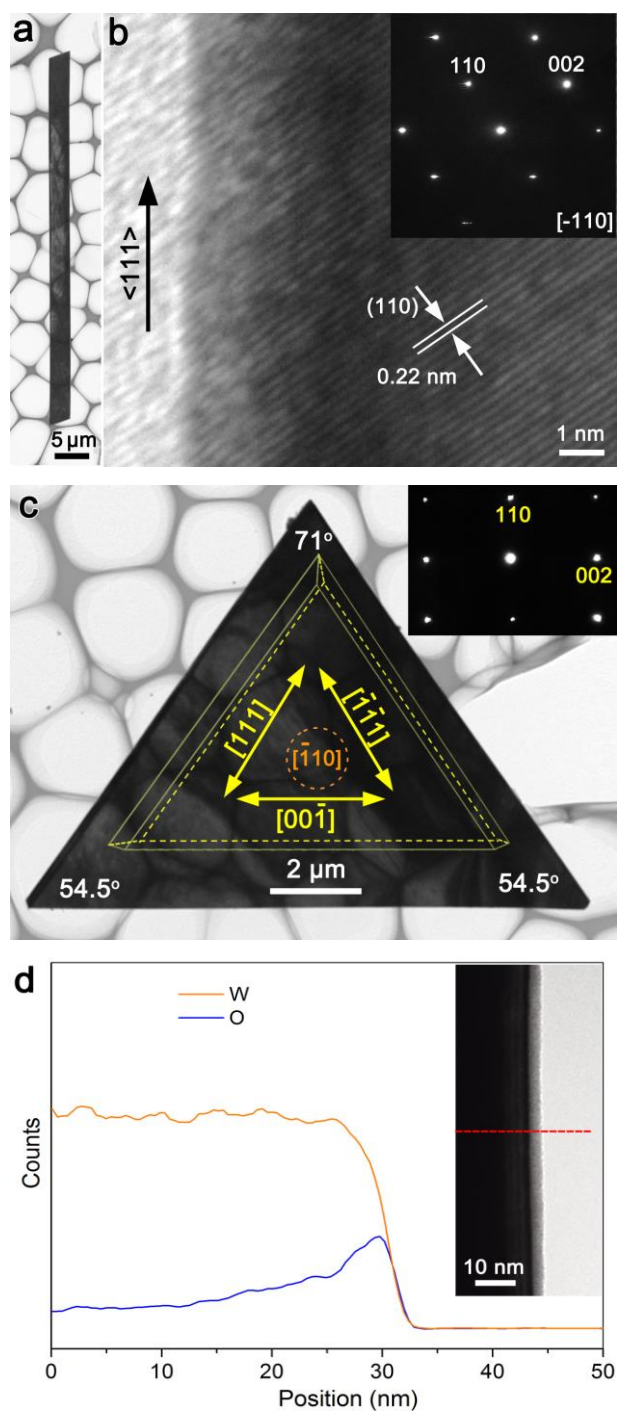
Fig. 2 (a) low-magnification and (b) high-resolution TEM images and the corresponding SAED pattern (the inset) of a parallelogram-like W nanobelt; (c) low-magnification TEM image and the corresponding SAED pattern (the inset) of a triangular W nanosheet; (d) the line-scan EDS spectrum recorded at the edge of a nanobelt (the inset). The sketch in (c) shows the 3D morphology of the triangular W nanobelt.
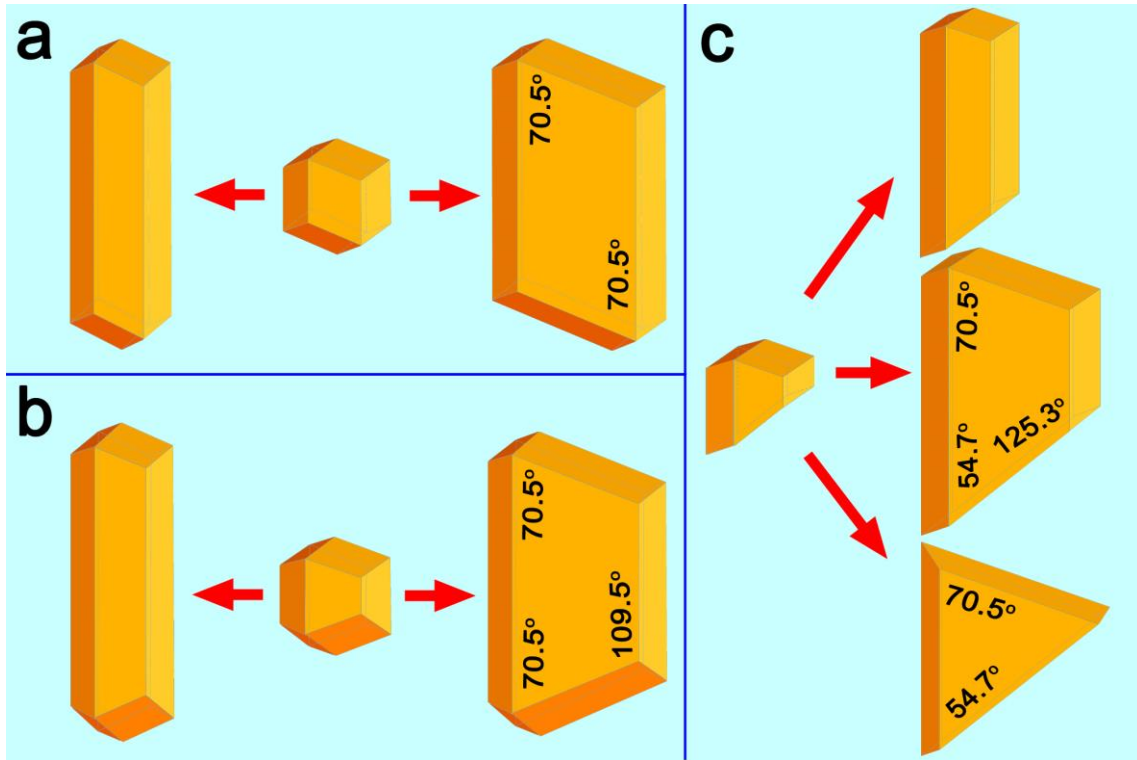
Fig. 3 The Wulff shapes of the bcc-W crystals enclosed by (a) 12 parallelograms, (b) 6 parallelograms and 6 isosceles trapezoids, (c) 7 parallelograms, 2 trapezoids and 1 hexagon.
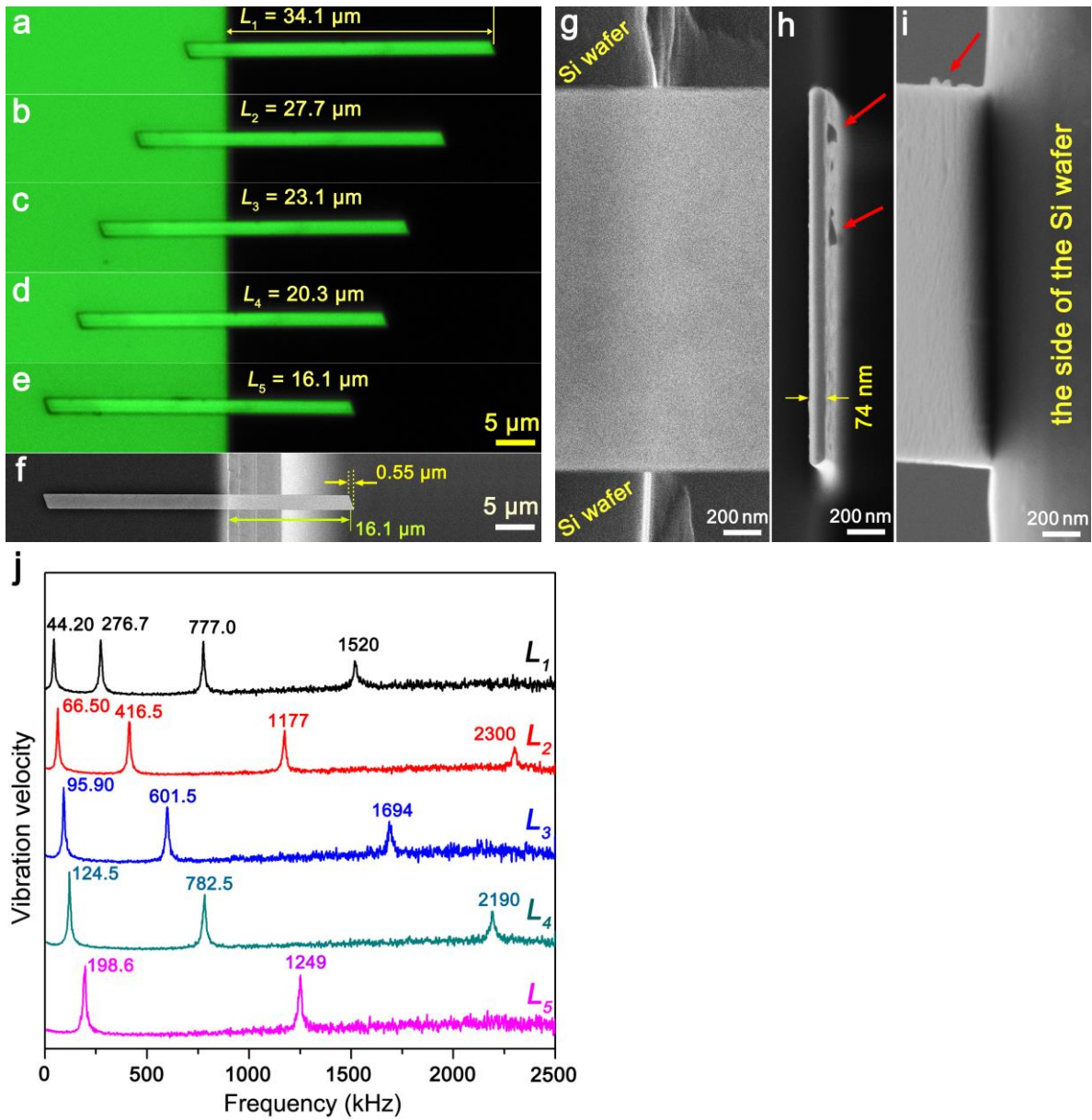
Fig. 4 (a-e) Optical micrographs of a nanobelt mounted at the edge of a Si wafer with five different lengths; f) SEM micrograph of the nanobelt shown in (e); g) top-view, h) end-view and i) bottom-view of the nanobelt shown in (e), respectively; (j) the vibrational spectra of the five cantilevers of different lengths shown in (a) - (e). The red arrows in (h) and (i) show the small contaminations attached to the nanobelt surface.
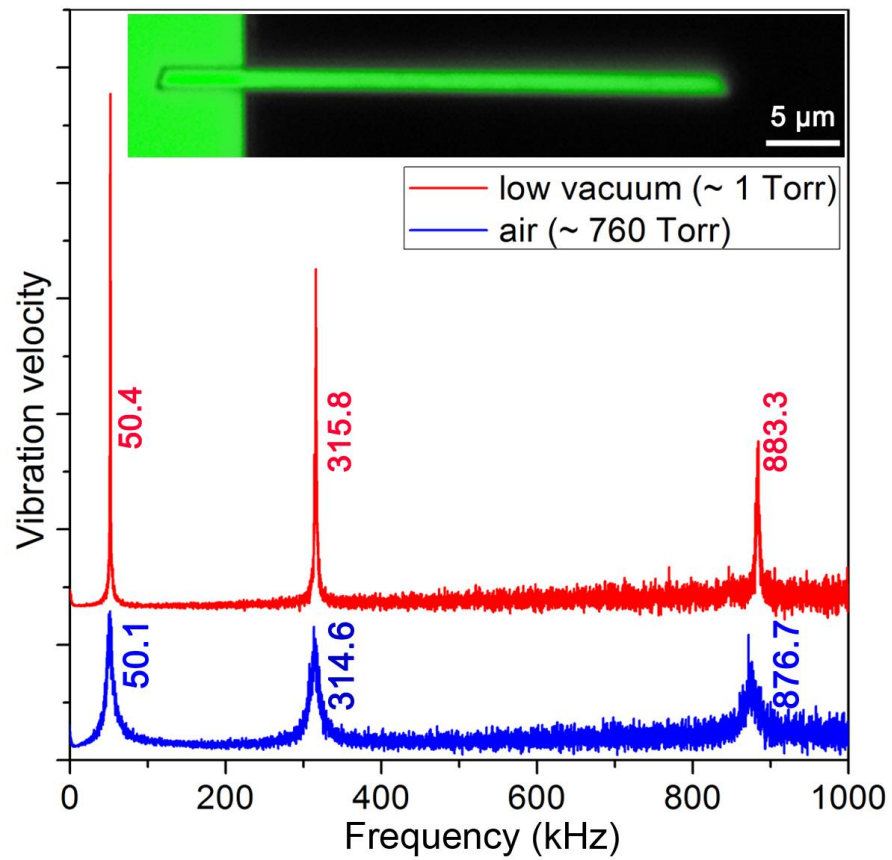
Fig. 5 The vibrational spectra of a nanobelt (shown in the inset) measured at ambient pressure (760 Torr) and low-vacuum (~ 1 Torr).
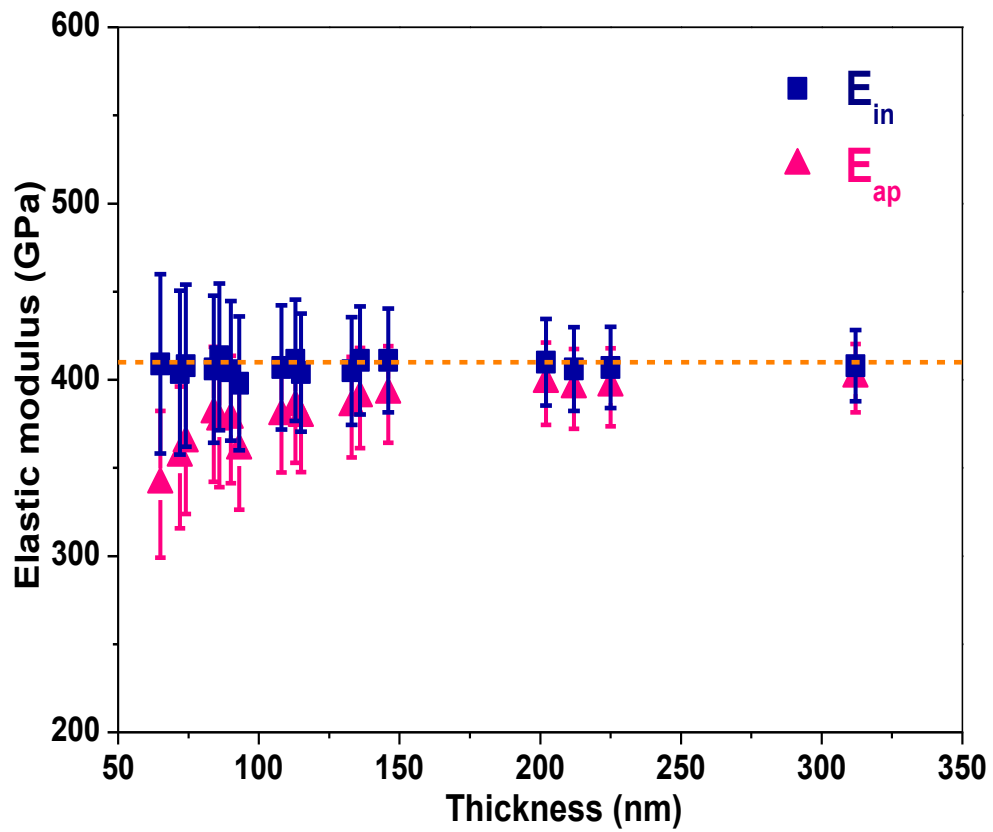
Fig. 6 The moduli, E_{ap}, obtained from the direct measurement and the intrinsic moduli, E_{in}, calculated by removing the effect of surface oxidation are plotted as a function of the nanobelts thickness.